PAPER • OPEN ACCESS

Spectrally red-shifted fluorescent fiducial markers for optimal drift correction in localization microscopy

IOP ebooks™

Bringing you innovative digital publishing with leading voices to create your essential collection of books in STEM research.

Start exploring the collection - download the first chapter of every title for free.

Spectrally red-shifted fluorescent fiducial markers for optimal drift correction in localization microscopy

Alexander Balinovic[1], David Albrecht[2] and Ulrike Endesfelder[1,3]

[1] Department of Systems and Synthetic Microbiology, Max Planck Institute for Terrestrial Microbiology and LOEWE Center for Synthetic Microbiology (SYNMIKRO), 35043 Marburg, Germany
[2] MRC Laboratory for Molecular Cell Biology, University College London, Gower Street, London WC1E 6BT, United Kingdom

E-mail: ulrike.endesfelder@synmikro.mpi-marburg.mpg.de

CrossMark

Abstract

Precise drift correction is crucial for every single-molecule localization-based microscopy experiment. We evaluate commonly used fiducial markers such as gold nanoparticles, TetraSpeck microspheres, FluoSpheres and nanodiamonds. We introduce spectrally red-shifted fluorescent particles as optimal fiducial markers. Our concept exploits exciting the fluorescent particles at low efficiency far away from their absorption maximum. A fluorescent particle that is covered by a multitude of dyes will nevertheless yield a bright fiducial signal. This represents a simple yet powerful approach to alleviate common problems in drift corrections caused by photobleaching, sudden signal intensity changes or saturation effects of fiducial markers. We adapt our approach for PALM, sptPALM and DNA-PAINT experiments and demonstrate its simple use for varying imaging conditions in different spectral channels.

S Supplementary material for this article is available online

(Some figures may appear in colour only in the online journal)

Introduction

Super-resolution microscopy revolutionized the life sciences as it allows unraveling the subcellular organization of live cells below the diffraction limit of light [1]. Among these techniques are the single-molecule localization microscopy (SMLM) methods which spatiotemporally separate and localize single molecules [2]. To record a sufficient number of individual molecular signals, SMLM imaging requires relatively long imaging sequences. Thus, drift caused by disturbances such as mechanical vibrations or thermal expansion is detrimental to image quality. This demands for highly stabilized microscopes that retain the probe at its position with sub-nanometer precision over the acquisition time. However, this is hardly achievable. Therefore, precise drift detection followed by drift correction is crucial, a circumstance that is widely appreciated in the SMLM community but rarely documented. Fundamentally, we differentiate between axial and lateral drift which can be corrected actively or passively. Active compensation relies on fast, counteracting closed-loop feedback systems during imaging. Passive compensation is achieved by an additional post-processing step during SMLM data analysis. To prevent axial drift, quadrant photodiode-based systems track the reflection of an infrared laser from the

---

[3] Author to whom any correspondence should be addressed.

J. Phys. D: Appl. Phys. **52** (2019) 204002

A Balinovic *et al*

coverslip surface [3, 4]. Implementations correcting for lateral drift and in some cases for axial drift either follow the position of fiducial markers or calculate spatial cross-correlations or statistical inference of the obtained images. The former method is based on fiducial markers placed within the sample or micropatterned onto the coverslip [3–11]. The latter method uses either (i) subsets of localized molecules at different time points [4, 12–15] or (ii) a second read-out channel which contains more detailed spatial information such as wide-field fluorescence images [16], bright field or infrared transmitted images [14, 17, 18], or phase contrast images of cellular outlines [19] which can be imaged in parallel or in alternation (e.g. every 20th frame) to the SMLM channel. Notably, drift correction via fiducial markers was the first [5, 6] and still is one of the most commonly used methods today, as it—in its simplest version—works without implementing any extra components to a standard fluorescence microscope and is—in contrast to correlative schemes—rather insensitive to molecule density or dynamics and independent from complex imaging sequences. Commonly used fiducial markers are gold nanoparticles [5, 10, 20], fluorescent beads [4, 6, 7, 9] and more recently nanodiamonds [21, 22]. In this paper, we compare the drift correction performance of these fiducial markers. We evaluate parameters like brightness and photostability of the fluorescent signal, and obstructions like aggregation artefacts and camera saturation. Furthermore, we propose a novel strategy which makes use of spectrally red-shifted fluorescent fiducial markers. With these, we yield a superior drift correction and show that our strategy is an improvement over existing schemes.

Materials and methods

Cell culture

Escherichia coli MG1655 rpoC-mEos3.2-A69T cells [23] from −80 °C stocks were cultured overnight at 37 °C, 210 rpm, LB with 34 μg ml^{-1} chloramphenicol, reinoculated 1:100 into EZ Rich Defined Medium (Teknova, USA) containing 2% glucose and grown at 37 °C, 210 rpm to OD 0.4.

Sample preparation for structural PALM imaging

8-well slides (Ibidi, Germany) were cleaned with 1M KOH, thoroughly washed with ultrapure water (Sigma-Aldrich, Germany) and coated with 0.05% poly-L-lysine (Sigma-Aldrich, Germany). Growing bacteria from EZ Rich Defined Medium were fixed with 2% *para*-formaldehyde (Sigma-Aldrich, USA) for 15 min, washed twice with 100 mM PBS (pH 7.4) and immobilized on cleaned 8-well slides. Fiducial markers (gold nanoparticles, 100 nm diameter, Sigma-Aldrich, Germany; TetraSpeck™ Microspheres, ThermoFisher, USA; FluoSphere dark red fluorescent Carboxylate-Modified Microspheres, ThermoFisher, USA; Carboxylate-modified medium bright red fluorescent Nanodiamonds, 100 nm, Adamas, USA) were sonicated by ultrasound (USC-TH, VWR, Germany) in their stock solution at 45 kHz for 5 min to avoid aggregates (the same settings were used for sptPALM and DNA-PAINT sample preparations), and added to the bacteria in a final 2000-fold dilution in PBS allowing them to settle for 20 min.

Sample preparation for sptPALM imaging

Microscopy slides (VWR, Germany) and cover glasses (Carl Roth, Germany) were cleaned with 1M KOH and thoroughly washed with ultrapure water (Sigma-Aldrich, Germany). Agarose pads (1% low gelling agarose, Sigma-Aldrich, USA) were placed on cleaned microscopy slides and allowed to solidify for 1.5 h. Sonicated fiducial markers (gold nanoparticles, 100 nm diameter, Sigma-Aldrich, Germany; TetraSpeck™ Microspheres, ThermoFisher, USA; FluoSphere dark red fluorescent Carboxylate-Modified Microspheres, ThermoFisher, USA; Carboxylate-modified medium bright red fluorescent Nanodiamonds, 100 nm, Adamas, USA) were added to the agarose pads and allowed to settle for 30 min. Growing bacteria from EZ Rich Defined Medium were washed twice with EZ Rich Defined Medium and were placed on the solidified agarose pads.

Sample preparation for DNA-PAINT imaging

E. coli MG1655 wildtype cells (laboratory Ding J. Jin, NIH, USA [24]) from −80 °C stocks were cultured overnight at 37 °C, 210 rpm, in LB medium, reinoculated 1:100, grown to OD 0.2, fixed with 2% *para*-formaldehyde (Sigma-Aldrich, USA) for 15 min, washed twice with 100 mM PBS (pH 7.4) and immobilized on cleaned 8-well slides (Ibidi, Germany) previously coated with 0.05% poly-L-lysine. Cells were permeabilized using 0.5% Triton-X solution (Sigma-Aldrich, USA), FluoSphere infrared fluorescent Carboxylate-Modified Microspheres (ThermoFisher, USA) were dispersed by ultrasound and added in a 2000-fold diluted solution to the sample allowing the fiducial markers to settle for 20 min. Prior to PAINT imaging, 400 pM JF646-Hoechst dye [25] was added to the sample.

Microscope setup

Imaging was performed on a custom build setup based on an automated Nikon Ti Eclipse microscope equipped with appropriate dichroic and filters (ET Dapi/Fitc/Cy3 dichroic, ZT405/488/561rpc rejection filter, ET595/50 bandpass, ET605/70 bandpass, ET610/75 bandpass, ET667/30 bandpass, BrightLine HC 676/29 bandpass, or BrightLine HC 689/23 bandpass, all AHF Analysentechnik, Germany), and a CFI Apo TIRF 100× oil objective (NA 1.49, Nikon). All lasers (405 nm OBIS, 561 nm OBIS, 640 nm OBIS; all Coherent Inc. USA) were modulated via an acousto-optical tunable filter (AOTF) (Gooch and Housego, USA). Fluorescence was detected by an emCCD (iXON Ultra 888, Andor, UK). The *z*-focus was controlled with a commercial perfect focus system (Nikon, Germany). Acquisitions were controlled by a customized version of Micro-Manager [26]. Live cell sptPALM experiments

J. Phys. D: Appl. Phys. **52** (2019) 204002

A Balinovic *et al*

were performed using a customized heating stage at 32 °C. Standard read-out parameters of the Andor camera were em-gain 300, pre-amp gain 2, 30 Mhz read-out speed, binning 1, vertical shift 1.13 μs and frame transfer mode, unless stated otherwise.

Structural PALM imaging

Fixed rpoC-mEos3.2-A69T MG1655 *E. coli* cells and fiducial markers were imaged for 5 min in HILO illumination mode [27]. Applied laser intensities were: 45 W cm^{-2} at 405 nm and 725 W cm^{-2} at 561 nm. Movies were recorded at 16 Hz with an exposure time of 60 ms per frame and pulsing the 405 nm laser every 10th imaging frame photoconverting new fluorophores. After PALM imaging, a bright light snapshot of all illuminated regions was recorded to obtain the bacterial cell shapes.

Live cell sptPALM imaging

Live rpoC-mEos3.2-A69T MG1655 *E. coli* cells and fiducial markers were imaged for 5 min in HILO illumination mode pulsing the 405 nm laser every 10th imaging frame like for the fixed samples. Applied laser intensities were: 45 W cm^{-2} at 405 nm and 725 W cm^{-2} at 561 nm. Movies were recorded at 33 Hz with an exposure time of 30 ms per frame to follow the fast diffusing RNA polymerases. After sptPALM imaging, a bright light snapshot of all illuminated regions was recorded to obtain the bacterial cell shapes.

DNA-PAINT imaging

Fixed MG1655-WT *E. coli* cells and fiducial markers were imaged under PAINT conditions for 5 min in HILO illumination mode. Applied laser intensity was: 750 W cm^{-2} at 640 nm. Movies were recorded at 16 Hz with an exposure time of 60 ms per frame. After PAINT imaging, a bright light snapshot of all illuminated regions was recorded to obtain bacterial cell shapes.

Post-processing and data analysis

For obtaining single-molecule localizations, rapidSTORM 3.3.1 [28] was used. Fiducial marker trajectories were extracted using custom-written scripts written for *Fiji software* (*ImageJ 1.51f*) [29] and plotted using OriginPro 9.4 software (Origin LAB Corporation, USA). The localization precision of selected individual fiducial markers was calculated by nearest neighbor based analysis (NeNA) [30] using a customized software written in Python 3.5. The precision of drift correction was measured by fitting the localization distributions of these markers after drift correction using four, six, eight, ten or twelve other fiducial markers to a Gaussian. Localizations of fluorescent protein signals of adjacent imaging frames were tracked together using the Kalman filtering routine implemented in rapidSTORM with the NeNA precision and a 3σ vicinity. Corrected SMLM image reconstructions at a

pixelsize of 10 nm were created in rapidSTORM and blurred by a Gaussian of 1σ using *Fiji* to match the visual appearance of the SMLM image with the obtained resolution. sptPALM data was tracked using a customized tracking software written in C++ and visualized by a customized software written in C++ (*swift*, unpublished), to filter for trajectories longer than 5 steps.
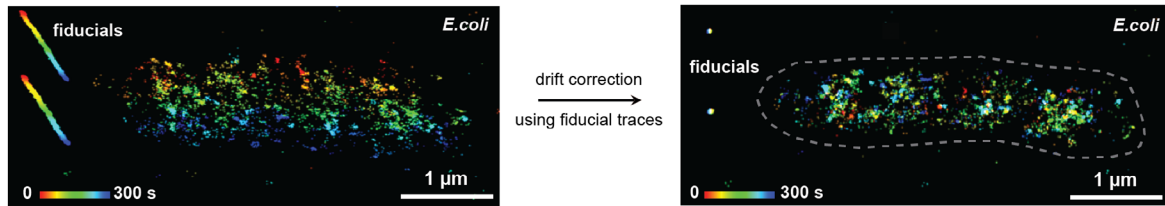
Spectroscopy

Excitation and emission spectra were measured using a FP-8500 spectrofluorometer (Jasco, Germany). Standard settings for the fluorometer were scan speed 100 nm min^{-1}, data interval 1 nm, excitation bandwidth 1 nm, emission bandwidth 10 nm. Scanning range for excitation spectra of mEos3.2-A69T, gold nanoparticles and TetraSpeck particles was 500–590 nm using a 600 nm emission read-out wavelength. Scanning range of excitation spectra for red FluoSpheres and nanodiamonds was 550–690 nm using a 700 nm emission read-out wavelength. Scanning range of excitation spectra for JF646-Hoechst was 600–690 nm using a 700 nm fluorescence read-out wavelength. Scanning range for infrared FluoSpheres was 600–780 nm with a 790 nm fluorescence read-out wavelength. Scanning range for emission spectra of mEos3.2-A69T, gold nanoparticles, TetraSpeck particles, red FluoSpheres and nanodiamonds was 550–750 using a 540 nm excitation wavelength. Scanning range for fluorescence spectra of JF646-Hoechst was 610–750 nm using a 600 nm excitation wavelength. Scanning range for fluorescence spectra of infrared FluoSpheres was 670–850 nm using a 650 nm excitation wavelength. JF646-Hoechst and all fiducial markers were diluted in 100 mM PBS (pH 7.4) at a final concentration of 1 μM. Purified mEos3.2-A69T fluorescent protein was measured at a final concentration of 100 μM in 100 mM PBS (pH 7.4). Spectra were baseline-corrected and plotted using OriginPro 9.4 software (Origin LAB Corporation, USA).
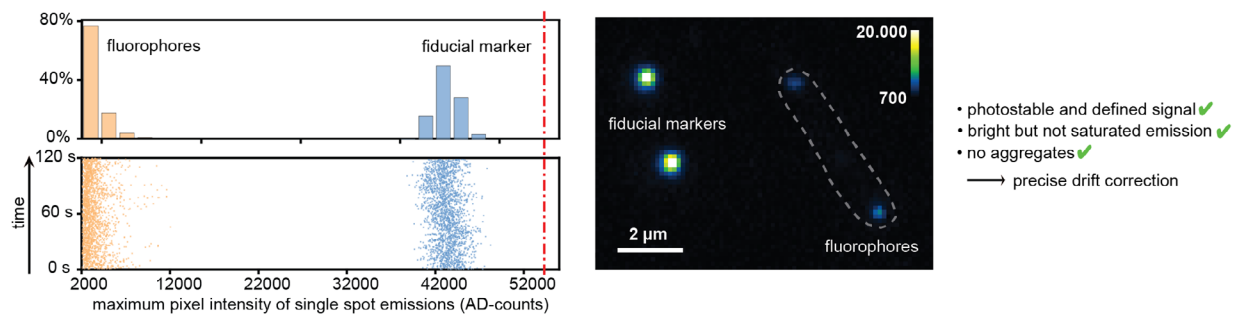
Results

Fiducial marker for precise drift correction (figure 1(a)) need to be spatially fixed landmarks within the sample that emit (i) a bright but non-saturated (supplementary note 1 at stacks.iop. org/JPhysD/52/204002/mmedia) and (ii) a photostable, non-fluctuating fluorescent signal throughout the SMLM imaging sequence and are (iii) monodispersed. Aggregates are usually much brighter than individual objects, often possess different photophysical properties (e.g. gold) and irregular shapes are poor to fit (figure 1(b)). For robust SMLM sample preparation and imaging routines, all of these criteria should be easily achievable. We characterized the performance of various commonly used fiducial markers by two test scenarios: structural photoactivated localization microscopy (PALM) imaging [5] of fixed samples to resolve the intracellular organization of molecules within cells and single-particle tracking PALM (sptPALM) imaging [31] of live samples to measure interaction dynamics of individual molecules (figures 1(c) and (d)). As a well-characterized biological test system we imaged
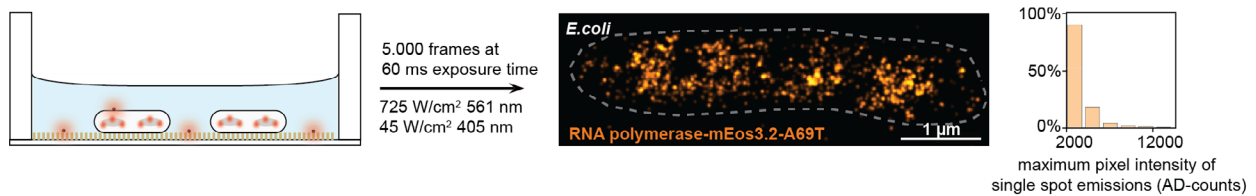
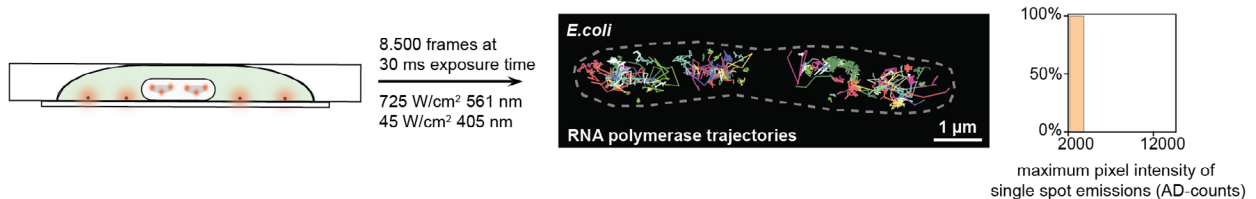J. Phys. D: Appl. Phys. **52** (2019) 204002

A Balinovic *et al*

Figure 1. (a) Exemplary SMLM image of the RNA polymerase distribution of an *E. coli* cell before and after drift correction using two fiducial markers which serve as landmarks during the five minutes long image acquisition. (b) Criteria for an optimal fluorescent marker for fiducial based drift correction in SMLM applications. The optimal fiducial marker exhibits brightness at the upper range of the dynamic range of the camera, has a stable and defined fluorescence signal over time without entering saturation and does not form aggregates. (c) and (d) Schematic representation of structural PALM imaging of RNA-polymerase endogenously tagged with mEos3.2-A69T in fixed *E. coli* cells in a multi-well chamber and dynamical sptPALM imaging of RNA-polymerase endogenously tagged with mEos3.2-A69T in live *E. coli* cells in an agarose pad using fluorescent fiducial markers as drift correction markers. After structural PALM imaging or dynamical sptPALM imaging under the displayed conditions, localizations of fitted single fluorescent spots are drift corrected and reconstructed into either a super-resolved image (c) or categorically color-coded trajectories of single RNA-polymerase molecules (d). Gray dashed lines highlight the bacterial cell walls. Orange bar plots display the distribution of the maximum pixel intensity of fluorescence signals of single mEos3.2-A69T molecules during PALM and sptPALM imaging in AD-counts.

E. coli RNA polymerase [32–36]. Here, we took advantage of our previously described strain where the endogenous rpoC gene was replaced by the fluorescent protein mEos3.2-A69T tagged version [23, 37]. We prepared samples following commonly applied SMLM protocols using either poly-L-lysine coated multi-well chambers for fixed cells or agarose pads for live cells (figures 1(c) and (d) and material and methods). The selected fluorophore mEos3.2-A69T is a bright, highly monomeric green-to-red photoconvertible fluorescent protein (red

chromophore ex/em 507/573 nm) from the class of Anthozoan fluorescent proteins [23]. On our microscope, we achieved a maximum pixel intensity of about 3500 AD-counts for single mEos3.2-A69T molecules (fixed cells) when using the most sensitive camera settings (materials and methods). An ideal fiducial marker should be detected in the upper part of the dynamic range of the camera. On our iXON Ultra 888 this corresponds to between 40.000 and 50.000 AD-counts (figure 1(b), supplementary note 1, supplementary figures 1 and 2).

J. Phys. D: Appl. Phys. **52** (2019) 204002

A Balinovic *et al*

Due to the faster read-out of sptPALM acquisitions, less photons are collected per fluorophore and imaging frame as seen in the histograms of intensity maxima of fluorescent spots for exemplary PALM and sptPALM measurement of mEos3.2-A69T (figures 1(c) and (d), right).

The first class of fiducial markers we tested are gold nanoparticles, which are available in different sizes (5–400 nm) and forms (beads, rods etc) [38, 39]. We chose 100 nm sized gold nanoparticles as their spectrum fits well to a laser excitation at 561 nm as well as to the read-out channel of mEos3.2-A69T. Recording spectra of gold nanoparticles and mEos3.2-A69T, we show that mEos3.2-A69T is almost perfectly excited with 98% absorption efficiency and that the used 610-75 bandpass filter (transmits emission of 572–648 nm) collects about 95% of the fluorescence signal. Together, this yields a read-out efficiency of about 93% of mEos3.2-A69T on our microscope. The 100 nm sized gold nanoparticles display an excitation efficiency of 56% at 561 nm with 70% of their emission signal being detected using the 610-75 bandpass filter. Taken together, this yields about 39% read-out efficiency (figure 2(a)). When immobilized on a multi-well chamber or in agarose pads, gold nanoparticles tend to form very bright, highly irregular shaped aggregates that bear the risk of entering saturation and imprecise localization estimation (figure 2(b)). Importantly, even prolonged sonication of gold nanoparticle solutions to disperse the particles did not fully prevent these aggregates. Nevertheless, the selected individual gold nanoparticles exhibit a stable signal over time (figure 2(c)). We did not observe many spikes of spontaneous intensity jumps for the individual particles as observed by others before for gold rods [22]. In our experiments, the pronounced occurrence of intensity spikes was only visible for aggregates (supplementary figure 3). Overall, gold nanoparticles only showed a slightly higher emission signal (3000–6000 AD-counts) compared to mEos3.2-A69T in both multi-well chambers and agarose pads (figure 2(d)). Taken together, this leads to a stable drift correction trace without any artificial offsets (e.g. caused by localization-artefacts of fiducial markers due to abrupt intensity changes, see results of TetraSpeck fiducial markers below) but at a low localization precision due to low signal. To evaluate the drift correction performance, we applied the trace obtained from four different single gold nanoparticles in a single field of view from a fixed sample onto a fifth single gold nanoparticle of the same field of view. We determined the Gaussian spread of the drift-corrected localizations of this fifth fiducial marker by taking the full width at half maxima (FWHM) in *x*- and *y*-dimension of the distribution. This yielded a resolution of 17.2 nm $\pm$ 0.4 nm in *x*-dimension and 18.1 nm $\pm$ 0.5 in *y*-dimension (figure 2(e)). The achievable resolution of the fiducial marker used for read-out of the quality of drift correction is limited to 2.35 times its localization precision. Thus, when we compared resolution to localization precision determined to 6.9 $\pm$ 0.3 nm by NeNA [30], we concluded that the drift correction performed optimally. However, its read-out is fundamentally limited by the low brightness of the gold nanoparticles. This result was confirmed when evaluating 20 more exemplary gold nanoparticles. The obtained Gaussian sigma after drift correction and

the NeNA localization precision values agreed with an average of 14.9 $\pm$ 2.9 nm (min/max 7.5/19.2) and 14.7 $\pm$ 3.3 nm (min/max 7.3/19.8), respectively (figure 2(f)).

The second class of fiducial markers we tested are fluorescent particles. For example, TetraSpeck™ Microspheres (ThermoFisher) are spherical polymer particles, labeled with four discrete fluorescent dyes (ex/em 360/430 nm; 505/515 nm; 560/580 nm; 660/680 nm). TetraSpeck particles are popular not only for drift correction but also serve as a reference for overlaying different spectral channels [40, 41]. The orange dye is perfectly suited for the spectral read-out channel of mEos3.2-A69T and our recorded spectra reveal an excitation efficiency of 98% and a fluorescence collection of 85% which together yield about 83% read-out efficiency for this dye (figure 3(a)). Notably, organic fluorescent dyes are usually several times brighter than fluorescent proteins [42]. TetraSpeck particles are coated with several dyes and are very bright. Therefore, at high laser intensities and high em-gain used to detect the rather weak signals from fluorescent proteins, the camera chip is easily saturated by TetraSpeck particles. To avoid damaging the camera detector, a typical work-around strategy in the SMLM field is to 'pre-bleach' the TetraSpeck particles until their signal is sufficiently reduced to match the dynamic range of the camera chip at the chosen settings for SMLM (personal communications). As a showcase, we recorded fluorescence signals of TetraSpeck particles immobilized on multi-well chambers, varying em-gain and pre-bleaching times and compared them to the fluorescence signal of mEos3.2-A69T and the background level (figure 3(b)). An em-gain of 3 is the lowest em-gain setting we can apply on our camera. Here, the TetraSpeck particles display about 30.000 AD-counts and the mEos3.2-A69T signal is not distinguishable from the background. This is not surprising, as typically an em-gain of 300 is used for SMLM imaging to distinguish mEos3.2-A69T or other fluorescent proteins from the background. However, increasing the em-gain above 3 caused the TetraSpeck particles to saturate the camera. Notably, we observed camera saturation at about 52.000 AD-counts (supplementary note 1). Increasing bleaching times of up to 15 min were required to avoid camera saturation (figure 3(b)). However, the requirement to pre-bleach the particles for 15 min prior to every SMLM imaging sequence is only justifiable for fixed cell studies where phototoxicity is irrelevant. It nevertheless massively increases experiment time and risks modifying the sample due to accumulated heat or by loss of information due to spontaneously photoconverted and photobleached fluorescent proteins during the 'pre-bleaching phase'. These aspects together question their use as fiducial markers in SMLM experiments. Positively, we found no tendency of the TetraSpeck particles to form aggregates (figure 3(c)) which is in contrast to the gold nanoparticles (figure 2(b)). When monitoring the intensity traces of different 'pre-bleached' particles over time, it became evident that their fluorescence signal is highly variable as it showed several spikes and discrete intensity jumps. We attribute this behavior to spontaneous photobleaching or blinking of single dye molecules which increases or decreases the fluorescence signal in discrete intensity steps (figures 3(d) and (e)). Based on the
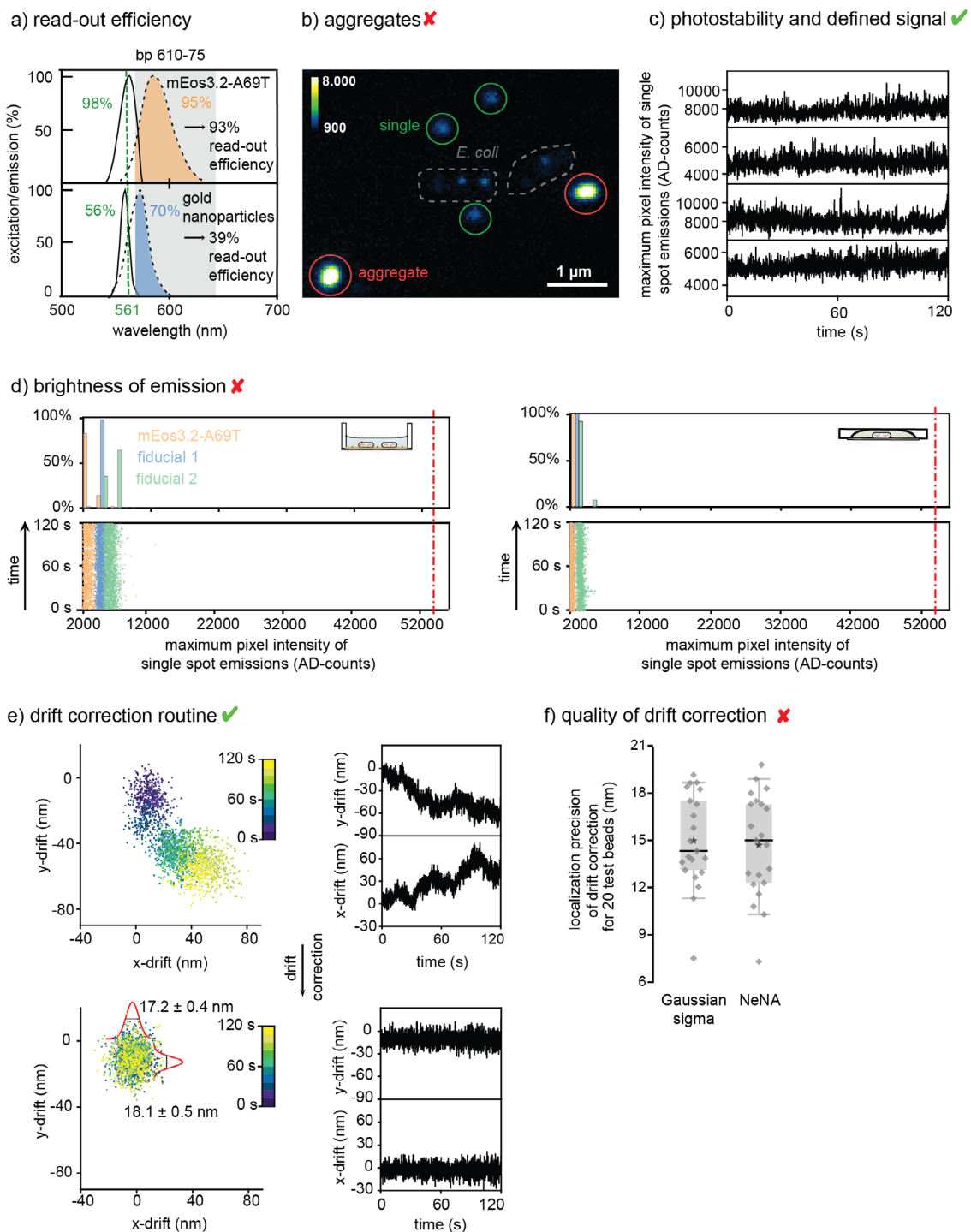
Figure 2. (a) Normalized excitation and emission spectra of mEos3.2-A69T and 100 nm sized gold nanoparticles. Green dashed line represents 561 nm excitation. Gray rectangle represents the detection window of the emission signal when using a 610-75 bandpass filter. Percentages of excitation efficiencies are color-coded in green, detection efficiency when using the 610-75 bandpass filter in orange (mEos3.2-A69T) and blue (gold particles). (b) PALM movie showing three dispersed gold nanoparticles, two gold particle aggregates and two *E. coli* cells with mEos3.2-A69T emissions within. (c) Four intensity traces of single gold nanoparticles from different regions of interest which exhibit stable and defined intensity. (d) Intensity traces of individual gold nanoparticles and mEos3.2-A69T proteins imaged with structural PALM (left panel) and sptPALM (right panel) utilizing a 610-75 bandpass filter. Blue and green data points and bar plots represent intensity traces of gold nanoparticles, orange data points and bar plots represent intensity traces of mEos3.2-A69T. Red dashed line marks the AD-count value where saturation is reached. (e) Localizations of an exemplary gold nanoparticle and corresponding drift traces in *x*- and *y*-dimension. Color scaling indicates the time point during image acquisition. Drift correction of this particle using four different gold nanoparticles yields a localization distribution with 17.2 ± 0.4 nm resolution in *x*-dimension and 18.1 ± 0.5 nm resolution in *y*-dimension, and a constant drift trace in both *x*- and *y*-dimension over time. Here, and in all further figures, the drift correction was performed with fiducial markers immobilized on poly-L-lysine surfaces. (f) Statistics of the achieved precision of drift correction by measuring the Gaussian sigma of 20 selected exemplary gold particles and NeNA localization precision values for the same particles.
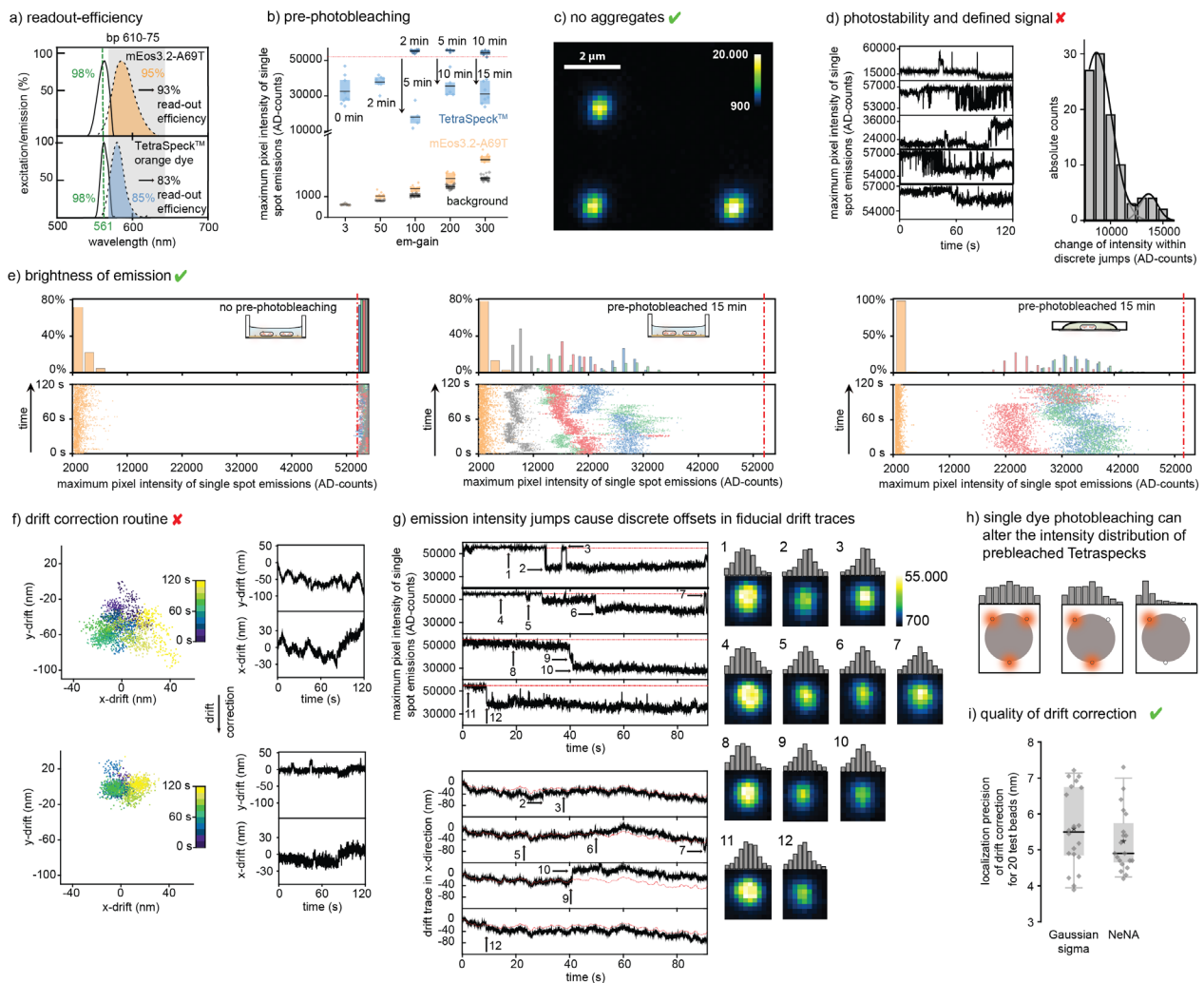
Figure 3. (a) Normalized excitation and emission spectra of mEos3.2-A69T and 100 nm sized TetraSpeck™ Microspheres. Green dashed line represents the excitation laser of 561 nm light. Gray rectangle represents the detection window of the emission signal when using a 610-75 bandpass filter. Percentages of absorption efficiencies are color-coded in green, detection efficiency when using the 610-75 bandpass filter in orange (mEos3.2-A69T) and blue (TetraSpeck particle). (b) TetraSpeck particle photobleaching. Red dotted line marks the AD-count value where saturation is reached. With an em-gain of 3, the TetraSpeck particle signals under PALM read-out do not enter saturation; however, mEos3.2-A69T signal is not distinguishable from background. By increasing the em-gain to 50, photobleaching for 2 min is required to retrieve TetraSpeck fluorescence below saturation. Further increase in em-gain to 100, 200 and 300 increases the needed pre-photobleaching times to 5, 10, and 15 min, respectively. When increasing the em-gain, the fluorescent protein signal becomes more distinguishable from background. (c) Exemplary image of a PALM movie of a region of interest containing individual TetraSpeck particles. No aggregation was observed. (d) Fluorescence intensity traces of five individual TetraSpeck particles, imaged under PALM conditions utilizing a 610-75 bandpass filter. TetraSpeck particles exhibit an unstable fluorescent signal with discrete fluctuations, often entering saturation. These discrete fluctuations can be accredited to single dye photobleaching or photoblinking events. When extracting the intensity differences from the jumps, single step and two step photobleaching of single dyes and dye pairs of respective ~7000 and ~14.000 AD-counts can be revealed. (e) Fluorescence intensity traces of individual TetraSpeck particles and mEos3.2-A69T imaged with structural PALM and sptPALM utilizing a 610-75 bandpass filter. Blue, green, gray, and red data points and bar plots represent fluorescence intensity traces of TetraSpeck particles, orange data points and bar plots represent fluorescence intensity traces of mEos3.2-A69T. Red dashed line marks the AD-count value where saturation is reached. The fluorescence signal of TetraSpeck particles is significantly distinguishable from the mEos3.2-A69T signal; however, pre-photobleaching for 15 min is necessary as the TetraSpeck signal enters saturation otherwise. Moreover, pre-photobleached TetraSpeck particles display discrete fluorescence intensity jumps in both, multi-well chambers and agarose pads. (f) Localizations of an exemplary TetraSpeck particle and corresponding drift traces in *x*- and *y*-dimension. Color scaling indicates the time point during image acquisition. Drift correction yields a non-spherical shaped localization distribution and a drift trace that still contains variations in both *x*- and *y*-dimension over time. (g) Correlation between fluorescence intensity jumps and drift correction offset. Significant jumps and offsets are highlighted by black arrows (left). Corresponding fiducial markers are pictured together with their profiles (right). (h) Explanatory scheme how photobleaching of single dye molecules can significantly alter the spatial intensity distribution of a single pre-bleached TetraSpeck particle. Grey circles mark an individual TetraSpeck particle, orange circles mark the fluorescent dyes. Bleaching of one or more fluorescent dyes significantly changes overall fluorescence distribution as seen in the profiles. (i) Statistics of the achieved precision of drift correction by measuring the Gaussian sigma of 20 selected exemplary TetraSpeck particles and NeNA localization precision values for the same particles.

observed discrete intensity steps, we can estimate the intensity of individual orange dyes to be 7000–8000 AD-counts. Thus, the orange dye incorporated into TetraSpeck particles is about 2–3 times brighter than mEos3.2-A69T (figure 3(d), right). We conclude that the brightest particles below saturation contain 6–8 non-bleached dyes on their surface. We observed this behavior in both multi-well chambers and agarose pads (figure 3(e)). The importance of a stable signal becomes striking when we evaluate the performance of the TetraSpeck particles in drift correction (figures 3(f) and (g)). Drift correction of an exemplary TetraSpeck particle using four different TetraSpeck particles yielded a non-circular localization distribution (figure 3(f)). Strikingly, this bias in drift correction appeared to be generated by the discrete fluorescence intensity jumps, which correlate with discrete jumps in the corresponding drift trace. The result is an offset of the individual drift trace to the overall drift correction trace (figure 3(g), left). Comparing the raw fluorescence images of several individual fiducial markers before and after these discrete intensity steps revealed a significant shift of the intensity maxima (figure 3(g), right). This behavior can be explained by the discrete and random distribution of the individual dyes on the surface of the TetraSpeck particle with a diameter of 100 nm. When bleaching one out of only few randomly distributed dye molecules on the microsphere, the overall fluorescence distribution may shift as sketched in figure 3(h). Our observations with TetraSpeck particles indicate that—next to their saturating brightness—a serious problem is bleaching and blinking under the high laser intensities used in SMLM imaging. However, the obtained drift correction quality can be improved to a certain extent when increasing the number of TetraSpeck particles as the larger statistics average out individual shifts contributing to the final drift trace. Correcting the exemplary TetraSpeck particle from figure 3(f) using four, eight and ten adjacent, pre-bleached TetraSpeck fiducial markers significantly improves the drift correction performance (supplementary figure 4(a(i)–(iv))) whereas increasing the number of fiducial markers from ten to twelve does not improve the drift correction any further (supplementary figure 4(a(v))). Here, the drastically from zero deviating remaining localization peaks in the *x*- and *y*-drift traces stem from mislocalization artifacts of the test particle itself and not from discrete shifts in the drift correction. This can be easily seen when comparing them to the corresponding original particle drift traces in *x*- and *y*-dimension (supplementary figure 4(a(vi))). When correcting another exemplary TetraSpeck particle of the same field of view using the exact same twelve fiducial markers, a circular localization distribution is obtained. Nevertheless, its overall resolution given by its Gaussian FWHM is still rather low at 11.7 ± 0.3 nm in *x*- and 11.4 ± 0.2 nm in *y*-direction. This indicates that the drift correction quality of pre-bleached TetraSpeck particles is—even when using a high number of fiducial markers—still limited by remaining errors in the drift trace due to individual mislocalizations as well as the limited brightness of pre-bleached TetraSpeck particles which additionally bleach further over the course of the experiment. For statistics, we selected 20 exemplary TetraSpeck particles which showed a by eye circular distribution of localizations

after drift correction (excluding those where the drift correction routine obviously failed as for the exemplary fiducial of figure 3(f)). For those, the obtained Gaussian sigma after drift correction and the NeNA localization precision values were similar and yielded an average of 5.6 ± 1.1 nm (min/max 3.9/7.2) and 5.2 ± 0.9 nm (min/max 4.2/7.3), respectively (figure 3(i)). Overall, this renders TetraSpeck particles rather unsuitable for robust drift correction in SMLM experiments: They require long pre-bleaching times and a high amount of fiducial markers to balance out localization shifts of individual particles due to blinking and bleaching events of single dyes. However, when read-out at intensities common in widefield or confocal fluorescence microscopy, TetraSpeck microspheres can serve as well-behaved fiducial markers for drift correction as well as for channel registration of multi-color applications.

In general, the fluorescence intensity of a particular fluorophore is the product of absorption efficiency and quantum yield at a certain excitation wavelength and intensity. As we cannot lower the laser intensity without sacrificing single-molecule signal, we figured that we could instead alter the absorption efficiency by shifting either the excitation wavelength or using fiducial markers with a different absorption spectrum. In this line of thought, a red dye would absorb the 561 nm laser needed for our PALM experiments significantly less efficient than an orange dye. We explored this option using dark red FluoSpheres (ThermoFisher, ex/em 660/680 nm). We measured the absorption spectrum upon excitation at 561 nm and determined an excitation efficiency of 1%. With our standard 610-75 bandpass filter we achieve 2% transmittance of the fluorescent signal. This was sufficient to saturate the camera under PALM conditions (figure 4(b), left, upper panel). For sptPALM, the signals were in the middle of the dynamical range of AD-counts per pixel, suitable for fiducial markers (figure 4(b), left, lower panel). Next, we tested different bandpass filters to optimize settings for PALM imaging. With a 605-70 bandpass filter, 0.7% of fluorescence was collected and yielded bright, non-saturated signals (figures 4(a) and (b), middle, 4(c)). With a 595-50 bandpass filter and 0.1% fluorescence collection efficiency, the FluoSphere signals dropped to the level of mEos3.2-A69T. These were too dim to still serve as robust fiducial markers (figures 4(a) and (b), right). The dark red FluoSpheres were monodispersed throughout the sample, thus did not form aggregates that could disturb measurements (figure 4(c)). With an excitation efficiency of 1%, the fluorescence signal from the dark red FluoSpheres was highly stable. We observed little variations caused by individual dye blinking and no photobleaching (figure 4(d)). Taken together, with the correct bandpass filter, the dark red FluoSpheres fulfill all criteria initially set out for an ideal fiducial marker when imaging the orange channel: They emit a (i) bright but non-saturated and a (ii) photostable and non-fluctuating fluorescent signal for long imaging periods and can be (iii) dispersed throughout the sample without forming aggregates. Consequently, the localization of one exemplary dark red FluoSphere using four different FluoSpheres yielded a localization distribution of 7.6 nm $\pm$ 0.1 nm and 7.7 nm $\pm$ 0.2 nm resolution in x- and *y*-dimension, respectively. This marks a significant improvement in drift correction compared to gold nanoparticles and
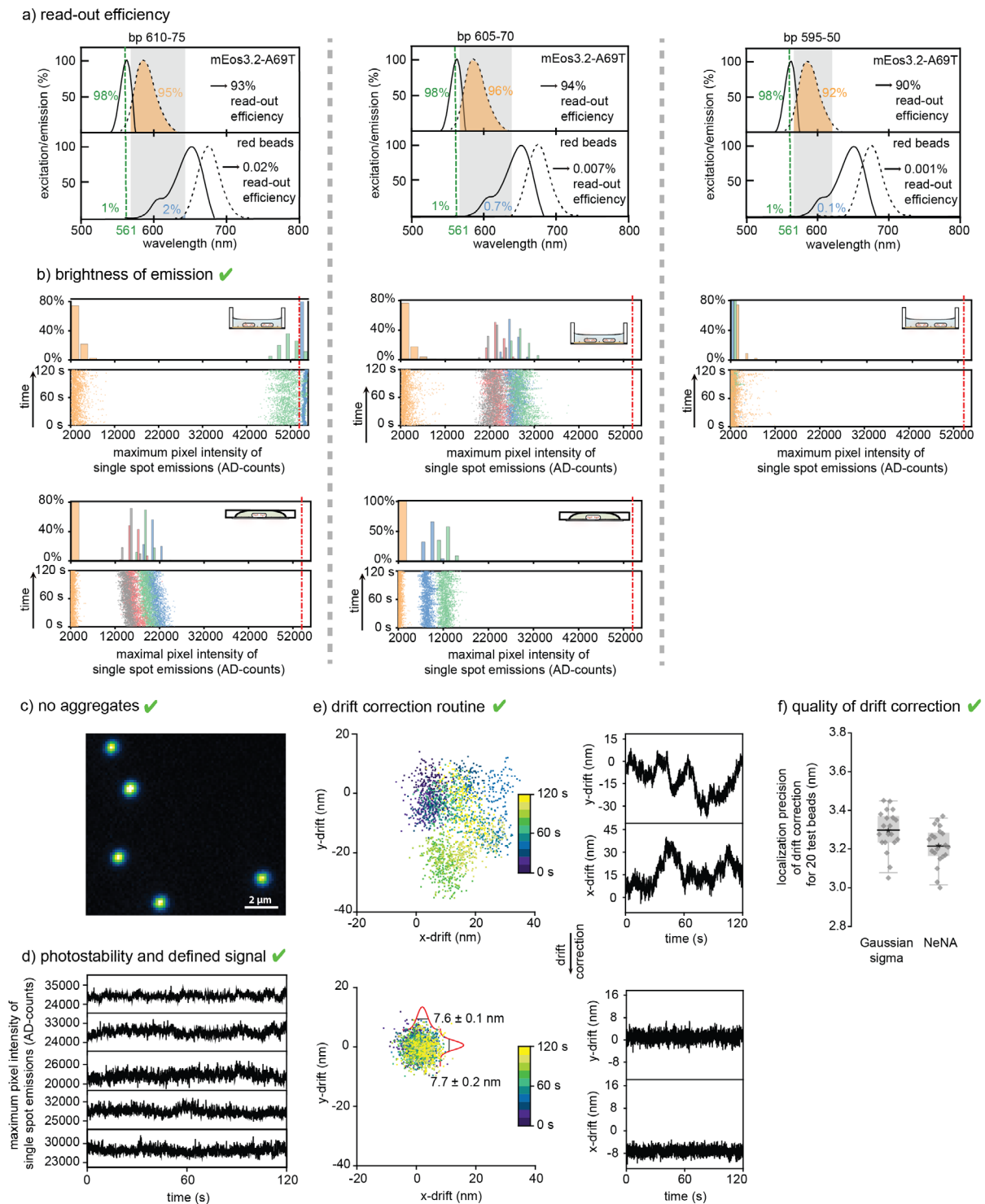
Figure 4. (a) Normalized excitation and emission spectra of mEos3.2-A69T and 200 nm sized red-fluorescent particles. Green dashed lines represent the excitation laser of 561 nm light. Gray rectangles represent the detection window of the emission signal when using a 610-75, 605-70 or 595-50 bandpass filter, respectively. Percentages of absorption efficiencies are color-coded in green, detection efficiency when using the respective bandpass filter in orange (mEos3.2-A69T) and blue (red FluoSpheres). (b) Fluorescence intensity traces of individual red FluoSpheres and mEos3.2-A69T proteins imaged with structural PALM and sptPALM utilizing a 610-75, 605-70 or 595-50 bandpass filter. Blue, green, gray, and red data points and bar plots represent fluorescence intensity traces of red FluoSpheres, orange data points and bar plots represent fluorescence intensity traces of mEos3.2-A69T. Red dashed line marks the AD-count value where saturation is reached. (c) Image from a PALM movie of a region of interest containing individual red FluoSpheres. No aggregate formation was observed. (d) Fluorescence intensity traces of five individual red FluoSpheres, imaged under PALM conditions utilizing a 605-70 bandpass filter. Red FluoSpheres exhibit a stable and defined fluorescence signal during image acquisition. (e) Localizations of an exemplary red FluoSphere and corresponding drift traces in *x*- and *y*-dimension. Color scaling indicates the time point during image acquisition. Drift correction yields a spherical shaped localization distribution with 7.6 ± 0.1 nm resolution in *x*-dimension and 7.7 ± 0.2 nm resolution in *y*-dimension, and a constant drift trace in both *x*- and *y*-dimension over time. (f) Statistics of the achieved precision of drift correction by measuring the Gaussian sigma of 20 selected exemplary FluoSpheres and NeNA localization precision values for the same particles.

J. Phys. D: Appl. Phys. **52** (2019) 204002

A Balinovic *et al*

TetraSpeck microspheres with a precision of about 3 nm (figure 4(e)). When performing drift correction for 20 different measurements, we determined an average precision of drift correction of 3.3 nm ± 0.1 nm (min/max 3.1/3.5 nm) localizing various drift-corrected test FluoSpheres. This is in agreement with the average NeNA localization precision of 3.2 ± 0.1 nm (min/max 3.1/3.4) (figure 4(f)).

By preparing a mixed sample using pre-bleached TetraSpeck particles and red FluoSpheres of similar intensity together, we directly compared the drift correction performance of both methods (supplementary figure 5). We picked an exemplary red FluoSphere to exclude artifacts stemming from the test particles' mislocalizations themselves as previously found for TetraSpeck particles (supplementary figure 5(i)) and performed drift correction using four, six, eight, ten and twelve pre-bleached TetraSpeck microspheres (supplementary figure 5(ii)) or four, six, eight, ten red FluoSpheres (supplementary figure 5(iii)). Whereas the drift correction using FluoSpheres yielded high quality when using only four particles and did not significantly improve further by increasing the number of correcting fiducial markers, the correction of the same test particle using the TetraSpeck particles did not reach a satisfactory quality for any number of used fiducial markers. This is nicely reflected by the again highly irregular intensity traces of the individual TetraSpeck particles (supplementary figure 5(iv)) whereas the red FluoSphere traces yielded a stable signal (supplementary figure 5(vi)). In conclusion, the spectrally red-shifted FluoSpheres yield a precise drift correction using only a few fiducial markers and their performance is superior to TetraSpeck particles.

The idea of spectrally red-shifted fiducial markers can of course be easily translated to other spectral channels. For the in SMLM imaging popular far-red dyes like Alexa Fluor 647, Cy5 or ATTO655 [1], an infrared colored fiducial fits the requirements. We therefore tested infrared FluoSpheres, ThermoFisher (ex/em 715/755 nm) using 640 nm laser excitation. As a biological sample we chose to resolve the nucleoid of *E. coli* cells by DNA-PAINT (figure 5(a)) using the far-red fluorescent organic dye JF646-Hoechst [25]. For 640 nm excitation, JF646 possesses an excitation efficiency of 88%, the infrared FluoSpheres of only 0.1%. Using a bandpass 676-29, 46% of JF646 fluorescence and 0.2% of the fluorescence of the infrared FluoSpheres were collected, yielding total efficiencies of 41% and 0.002%, respectively (figure 5(b)). As all tested polymer microspheres, the infrared FluoSpheres were monodispersed on the sample and did not form aggregates (figure 5(c)). The fluorescence signal under 640 nm excitation was stable and without any intensity jumps (figure 5(d)). Even though the chosen bandpass filter is rather narrow and cuts a significant fraction of the JF646 signal, it was the best compromise among the currently available filters, as other tested bandpass filters either led to camera saturation (bandpass 689-23) or diminished the fiducial marker signal (bandpass 667-30) (figure 5(e)). After optimization, we achieved good drift correction and robust results as seen for the exemplary drift trace in figure 5(f) with a resolution of 9.2 ± 0.1 nm and 8.6 ± 0.1 nm in *x*- and *y*-dimension and thus a precision of about 3.8 nm. When evaluated for 20 different measurements,

we obtained an average drift correction precision of 3.5 ± 0.3 nm (min/max 2.85/4.2 nm), and an average NeNA localization precision of 3.5 ± 0.3 nm (min/max 3.0/3.9) (figure 5(g)). Overall, this confirms the utility of red-shifted fiducial markers for drift correction.

Recently, fluorescent nanodiamonds were introduced as fiducial markers. Nanodiamonds display a superior drift correction quality when compared to gold nanoparticles and fluorescent particles due to their stable emission and high brightness [21, 22]. We tested far-red-emitting nanodiamonds under typical SMLM imaging laser excitation. The nanodiamonds saturated the camera chip when used in their 'correct' far-red color channel, i.e. at high excitation efficiencies. We therefore explored their use as red-shifted fiducial markers similar to above described FluoSpheres. When excited using a 561 nm laser, the nanodiamonds displayed a relatively low excitation efficiency of 0.5% and a signal collection efficiency of 0.3% with the 610-75 bandpass filter. Together, this resulted in a read-out efficiency of 0.0015% (figure 6(a)). Unfortunately, we observed aggregate formation of the nanodiamonds as seen with gold nanoparticles (figure 6(b)). Single nanodiamond particles displayed a photostable signal (figure 6(c)). Used as red-shifted fiducial markers, they were brighter than gold nanoparticles but not as bright as the red-shifted FluoSpheres (figure 6(d)). This directly transferred into drift correction performance. We achieved a localization precision of about 6 nm, as seen for the drift corrected nanodiamond in figure 6(e) with a resolution of the localization distribution of 14.4 ± 0.4 nm and 14.0 ± 0.4 nm in *x*- and *y*-dimension, respectively. Evaluation of drift correction of 20 measurements yielded an average drift precision of 9.5 ± 2.1 nm (min/max 6.0 nm/14.8), and a NeNA localization precision of 9.7 ± 2.3 nm (min/max 6.6/15.0).

In a final step, we performed a comparative study of all fiducial markers for the mEos3.2-A69T channel and prepared mixed slides of each fiducial marker (gold particles, TetraSpeck particles and nanodiamonds) together with red FluoSpheres (figure 7). To validate the drift correction performance for each type of fiducial markers tested, we—like before—used each four fiducial markers to extract a drift correction trace. In contrast to the previous experiments though, we then applied this trace to red FluoSpheres as exemplary test beads. As such, the influence of variations in localization precision of different types of exemplary test beads can be neglected (as the red FluoSpheres showed a stable, bright signal which led to the highest precision values of all fiducial markers tested, see statistics figures 2–4). Here, we speculated that we might have underestimated the quality of drift correction using different fiducial markers as read-out particles earlier as averaged drift correction traces might have higher precisions than seen through the precision of the localizations of individual particles themselves. We thus expected that the drift-corrected localization distributions of red FluoSpheres as test particles might show a narrower Gaussian distribution than measured before when using the different types of fluorophores as test beads. First, we checked if we obtained fair comparative statistics for all chosen, individual test beads (all red FluoSpheres) in all samples: Indeed, the red FluoSpheres from different samples showed highly similar
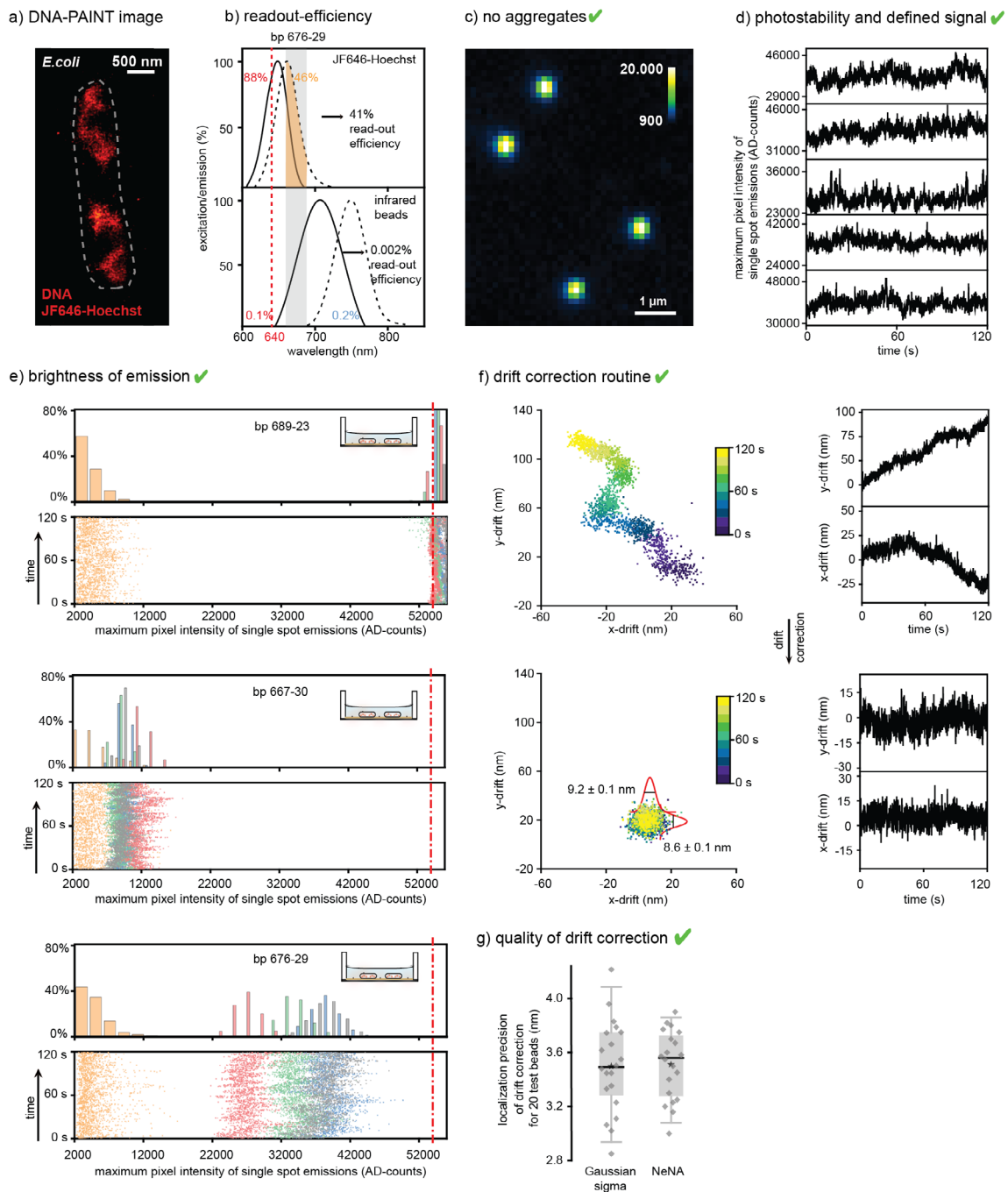
Figure 5. (a) Drift corrected DNA-PAINT image of a MG1655 wildtype *E. coli* cell, where the nucleoid is visualized using JF646-Hoechst. Gray dashed line highlights bacterial cell wall. Drift correction was performed using infrared FluoSpheres. (a) Normalized excitation and emission spectra of mEos3.2-A69T and 100 nm sized infrared-fluorescent particle. Red dashed line represents the 640 nm excitation laser. Gray rectangle represents the detection window of the emission signal when using a 676-29 bandpass filter. Percentages of absorption efficiencies are color-coded in red, detection efficiency when using the respective bandpass filter in orange (mEos3.2-A69T) and blue (infrared FluoSpheres). (c) Exemplary image of a DNA-PAINT movie of a region of interest containing individual infrared FluoSpheres. No aggregate formation was observed. (d) Fluorescence intensity traces of five individual infrared FluoSpheres, imaged under PAINT conditions utilizing a 676-29 bandpass filter. Infrared FluoSpheres exhibit a stable and defined fluorescence signal during image acquisition. (e) Fluorescence intensity traces of individual infrared FluoSpheres and JF646-Hoechst imaged with PAINT utilizing a 689-23, 667-30 or 676-29 bandpass filter. Blue, green, gray, and red data points and bar plots represent fluorescence intensity traces of infrared FluoSpheres, orange data points and bar plots represent fluorescence intensity traces of JF646-Hoechst. Red dashed line marks the AD-count value where saturation is reached. (f) Localizations of an exemplary infrared FluoSphere and corresponding drift traces in *x*- and *y*-dimension. Color scaling indicates the time point during image acquisition. Drift correction yields a spherical shaped localization distribution with 9.2 ± 0.1 nm resolution in *x*-dimension and 8.6 ± 0.1 nm resolution in *y*-dimension, and a constant drift trace in both *x*- and *y*-dimension over time. (f) Statistics of the achieved precision of drift correction by measuring the Gaussian sigma of 20 selected exemplary infrared FluoSpheres and NeNA localization precision values for the same particles.
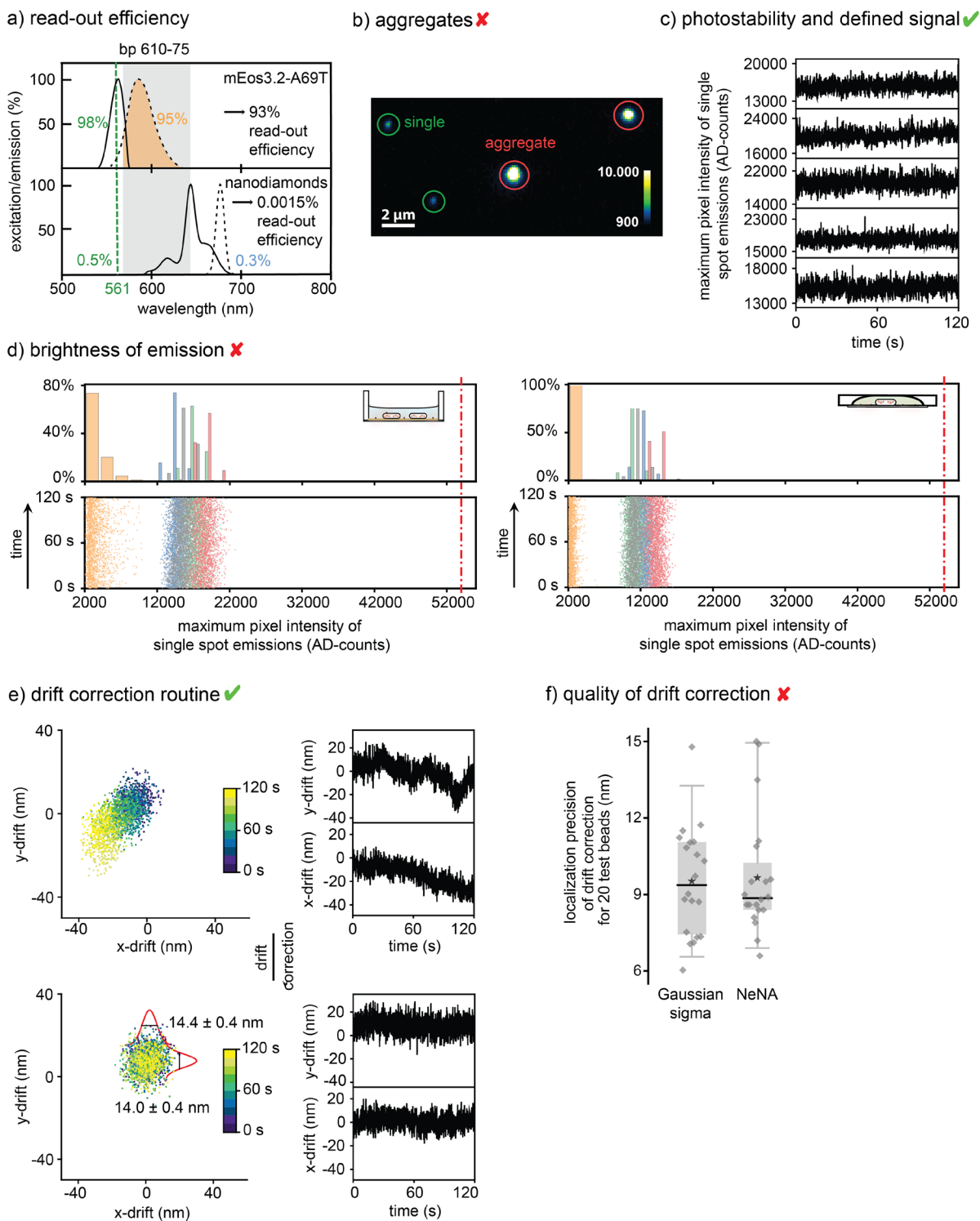
J. Phys. D: Appl. Phys. **52** (2019) 204002

A Balinovic *et al*

Figure 6. (a) Normalized excitation and emission spectra of mEos3.2-A69T and 100 nm sized red-fluorescent nanodiamonds. Green dashed lines represent the excitation laser of 561 nm light. Gray rectangles represent the detection window of the emission signal when using a 610-75 bandpass filter. (b) Exemplary image of a PALM movie of a region of interest containing nanodiamonds. Green circle highlights a single nanodiamond particle, red circle highlights a nanodiamond aggregate. (c) Fluorescence intensity traces of five individual nanodiamond particles, imaged under PALM conditions utilizing a 610-75 bandpass filter. Nanodiamond particles exhibit a stable and defined fluorescence signal during image acquisition. (d) Fluorescence intensity traces of individual nanodiamond particles and mEos3.2-A69T proteins imaged with structural PALM and sptPALM utilizing a 610-75 bandpass filter. Blue, green, gray, and red data points and bar plots represent fluorescence intensity traces of the nanodiamonds, orange data points and bar plots represent fluorescence intensity traces of mEos3.2-A69T. Red dashed line marks the AD-count value where saturation is reached. (e) Localization distribution of an exemplary nanodiamond particle and corresponding drift traces in *x*- and *y*-dimension. Color scaling indicates the time point during image acquisition. Drift correction yields a spherical shaped localization distribution with 14.4 ± 0.4 nm resolution in *x*-dimension and 14.0 ± 0.4 nm resolution in *y*-dimension, and a constant drift trace in both *x*- and *y*-dimension over time. (f) Statistics of achieved precision of drift correction by measuring the Gaussian sigma of 20 selected exemplary nanodiamonds and NeNA localization precision values for the same particles.
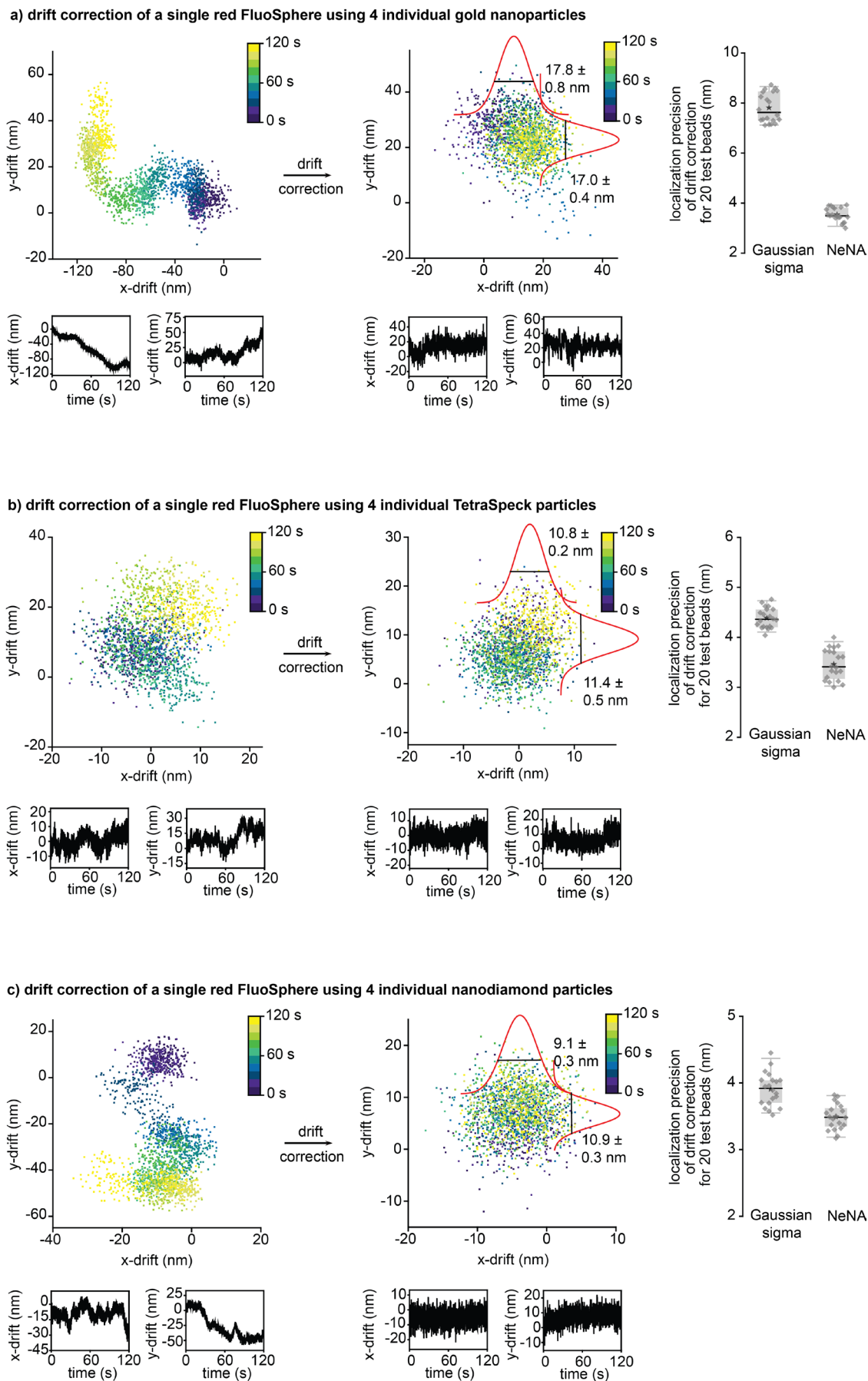
a) drift correction of a single red FluoSphere using 4 individual gold nanoparticles

b) drift correction of a single red FluoSphere using 4 individual TetraSpeck particles

c) drift correction of a single red FluoSphere using 4 individual nanodiamond particles

Figure 7. Exemplary drift correction of an individual test bead and statistics for 20 red FluoSphere particles using drift correction traces calculated from each four gold particles (a), four pre-bleached TetraSpeck particles (b) or four nanodiamonds (c).

J. Phys. D: Appl. Phys. **52** (2019) 204002

A Balinovic *et al*

Table 1. Summarizing overview of the performance of the different fiducial markers for drift correction in SMLM experiments. Only the spectrally red-shifted FluoSpheres fulfil all criteria for optimized drift correction quality as they exhibit a bright and photostable fluorescence signal while forming no aggregates.

	Brightness	Monodispersion	Photostability	Drift correction
Spectrally-red shifted FluoSpheres	✓	✓	✓	✓
Spectrally-red shifted nanodiamonds	×	×	✓	✓
TetraSpeck microspheres	×	✓	×	×
Gold nanoparticles	×	×	✓	✓

NeNA localization precision values of on average 3.5 ± 0.3 nm, min/max 3.0/3.9 nm (figure 7(a), mixture with gold particles), 3.5 ± 0.3 nm, min/max 3.0/4.0 nm (figure 7(b), mixture with TetraSpeck particles) and 3.5 ± 0.2 nm, min/max 3.2/3.8 nm (figure 7(c), mixture with nanodiamonds). We then looked at the Gaussian sigma marking the quality of drift correction of each four fiducial markers on each one red FluoSphere to compare the performance of the different fiducial markers without being biased by their own and in particular different localization imprecisions. The obtained Gaussian sigma values were significantly lower than before (confirming the influence of the test bead resolution itself on the values before), but the differences in drift correction quality were still clearly detectable with averages of 7.8 ± 0.6 nm, min/max 7.1/8.7 nm for the gold nanoparticles (figure 7(a)), 4.4 ± 0.2 nm, min/max 4.0/4.8 nm for the TetraSpeck particles (again, only by eye circular-shaped, drift-corrected test beads were selected, figure 7(b)) and 3.9 ± 0.2 nm, min/max 3.5/4.5 nm for the nanodiamonds (figure 7(c)). In conclusion, all of the different fiducial markers had a lower quality in drift correction when compared to the correction using each four red FluoSpheres (3.3 nm ± 0.1 nm; min/max 3.1/3.5 nm, figure 4(e)). Taken together, this behavior correlates with the average brightness and signal stability obtained for the different fiducial markers (figures 2–7). We prepared a table of the fiducial markers' performances for SMLM imaging (table 1). An additional overview summarizing our recommended filter settings can be found in supplementary table S1.

Conclusions

In this work, we compared the performance of different fiducial markers for drift correction in SMLM applications. For characterizing their performance, we first measured their excitation and emission spectra. Based on these we determined their read-out efficiencies in SMLM experiments with different emission bandpass filters. We performed structural PALM experiments imaging RNA-polymerase being endogenously tagged with mEos3.2-A69T of fixed *E. coli* in multi-well chambers and dynamic sptPALM experiments of live *E. coli* cells with the same target in agarose pads. For all fiducial markers, we determined brightness and photostability as well as their tendency to aggregate to finally perform drift correction evaluating the obtained resolution and localization precision.

We could demonstrate that fiducial markers such as gold nanoparticles, nanodiamonds and TetraSpeck microspheres display several draw backs. Gold or diamond nanoparticles tend to form aggregates even after sonication. TetraSpeck particles and nanodiamonds are too bright for a direct read-out in their color channel, gold particles tend to be too dim and their aggregates tend to blink heavily. The commonly used strategy to 'pre-bleach' TetraSpeck particles leads to microspheres covered by few fluorescent dyes, which strongly affects the drift traces due to discrete single step photobleaching or photoblinking events of individual dyes—even when utilizing a multitude of TetraSpeck particles to balance out individual intensity jumps. However, spectrally red-shifted fluorescent fiducial markers, such as red FluoSpheres or nanodiamonds observed in the orange spectral read-out channel or infrared FluoSpheres imaged in the far-red channel yield reliable and accurate drift correction. These fulfil all criteria that are required for an optimal fiducial marker: They are bright, photostable and—in case of the fluorescent polymers—do not show any formation of aggregates. Thus, spectrally red-shifted fluorescent particles are an ideal choice as fiducial markers for structural and dynamic SMLM experiments. This concept can be applied to any spectral channel and only needs a suitable bandpass filter. For example, we recommend using the 610-75 bandpass filter for agarose pad preparations and fast sptPALM imaging and the 605-70 bandpass filter for fixed cells in multi-well chambers and structural PALM imaging. In the far-red channel we achieved good results with a 676-29 bandpass. Theoretically, this concept could also be applied to TetraSpeck microspheres. However, as they are coated by four spectrally close fluorescent dyes matching the most commonly used spectral ranges and channels in fluorescence microscopy, the options to apply this concept for TetraSpeck particles are rather limited. Finally, the use of fiducial markers is common in the field and often preferred over integrating complex active stabilization elements into the optical system. An advantage over correlation-based methods is that fiducial markers work independently of sample features and thus do not require faithful detection of structural details. In our opinion, exploiting low excitation efficiencies of red-shifted fiducial markers is a simple yet powerful addition to current drift correction methods. We are convinced that this strategy will find multiple applications in future SMLM studies as it alleviates the common problems caused by photobleaching, aggregates, sudden signal intensity changes or saturation effects of fiducial markers.

Acknowledgements

J. Phys. D: Appl. Phys. **52** (2019) 204002

A Balinovic *et al*

ORCID iDs

David Albrecht ● https://orcid.org/0000-0001-9455-1134
Ulrike Endesfelder ● https://orcid.org/0000-0002-7801-6278

References

[1] Turkowyd B, Virant D and Endesfelder U 2016 From single molecules to life: microscopy at the nanoscale *Anal. Bioanal. Chem.* **408** 6885–911

[2] Endesfelder U 2016 Photoswitching fluorophores in super-resolution fluorescence microscopy *Super-Resolution Imaging in Biomedicine* (Boca Raton, FL: CRC) p 49

[3] Carter A R *et al* 2007 Stabilization of an optical microscope to 0.1 nm in three dimensions *Appl. Opt.* **46** 421–7

[4] Huang B *et al* 2008 Three-dimensional super-resolution imaging by stochastic optical reconstruction microscopy *Science* **319** 810–3

[5] Betzig E *et al* 2006 Imaging intracellular fluorescent proteins at nanometer resolution *Science* **313** 1642–5

[6] Rust M J, Bates M and Zhuang X 2006 Sub-diffraction-limit imaging by stochastic optical reconstruction microscopy (STORM) *Nat. Methods* **3** 793–5

[7] Pertsinidis A, Zhang Y X and Chu S 2010 Subnanometre single-molecule localization, registration and distance measurements *Nature* **466** 647–51

[8] Lee S H *et al* 2012 Using fixed fiduciary markers for stage drift correction *Opt. Express* **20** 12177–83

[9] Zessin P J *et al* 2013 A hydrophilic gel matrix for single-molecule super-resolution microscopy *Opt. Nanoscopy* **2** 4

[10] Bon P *et al* 2015 Three-dimensional nanometre localization of nanoparticles to enhance super-resolution microscopy *Nat. Commun.* **6** 7764

[11] Youn Y *et al* 2018 Thermal nanoimprint lithography for drift correction in super-resolution fluorescence microscopy *Opt. Express* **26** 1670–80

[12] Mlodzianoski M J *et al* 2011 Sample drift correction in 3D fluorescence photoactivation localization microscopy *Opt. Express* **19** 15009–19

[13] Geisler C *et al* 2012 Drift estimation for single marker switching based imaging schemes *Opt. Express* **20** 7274–89

[14] Tang Y *et al* 2014 Sub-nanometer drift correction for super-resolution imaging *Opt. Lett.* **39** 5685–8

[15] Elmokadem A and Yu J 2015 Optimal drift correction for superresolution localization microscopy with bayesian inference *Biophys. J.* **109** 1772–80

[16] Bates M *et al* 2007 Multicolor super-resolution imaging with photo-switchable fluorescent probes *Science* **317** 1749–53

[17] Mennella V *et al* 2012 Subdiffraction-resolution fluorescence microscopy reveals a domain of the centrosome critical for pericentriolar material organization *Nat. Cell Biol.* **14** 1159

[18] McGorty R, Kamiyama D and Huang B 2013 Active microscope stabilization in three dimensions using image correlation *Opt. Nanoscopy* **2** 1–7

[19] Holden S J *et al* 2014 High throughput 3D super-resolution microscopy reveals Caulobacter crescentus *in vivo* Z-ring organization *Proc. Natl Acad. Sci. USA* **111** 4566–71

[20] York A G *et al* 2011 Confined activation and subdiffractive localization enables whole-cell PALM with genetically expressed probes *Nat. Methods* **8** 327–33

[21] Colomb W *et al* 2017 Estimation of microscope drift using fluorescent nanodiamonds as fiducial markers *J. Microsc.* **266** 298–306

[22] Yi J *et al* 2016 madSTORM: a superresolution technique for large-scale multiplexing at single-molecule accuracy *Mol. Biol. Cell* **27** 3591–600

[23] Turkowyd B *et al* 2017 A general mechanism of photoconversion of green-to-red fluorescent proteins based on blue and infrared light reduces phototoxicity in live-cell single-molecule imaging *Angew. Chem., Int. Ed. Engl.* **56** 11634–9

[24] Cabrera J E and Jin D J 2003 The distribution of RNA polymerase in *Escherichia coli* is dynamic and sensitive to environmental cues *Mol. Microbiol.* **50** 1493–505

[25] Legant W R *et al* 2016 High-density three-dimensional localization microscopy across large volumes *Nat. Methods* **13** 359–64

[26] Edelstein A *et al* 2010 Computer control of microscopes using microManager *Current Protocols in Molecular Biology* ch 14, p Unit14 20

[27] Tokunaga M, Imamoto N and Sakata-Sogawa K 2008 Highly inclined thin illumination enables clear single-molecule imaging in cells *Nat. Methods* **5** 159–61

[28] Wolter S *et al* 2012 rapidSTORM: accurate, fast open-source software for localization microscopy *Nat. Methods* **9** 1040–1

[29] Schindelin J *et al* 2012 Fiji: an open-source platform for biological-image analysis *Nat. Methods* **9** 676–82

[30] Endesfelder U *et al* 2014 A simple method to estimate the average localization precision of a single-molecule localization microscopy experiment *Histochem. Cell Biol.* **141** 629–38

[31] Manley S *et al* 2008 High-density mapping of single-molecule trajectories with photoactivated localization microscopy *Nat. Methods* **5** 155–7

[32] Stracy M *et al* 2015 Live-cell superresolution microscopy reveals the organization of RNA polymerase in the bacterial nucleoid *PNAS* **112** E4390–9

[33] Spahn C *et al* 2015 Correlative super-resolution imaging of RNA polymerase distribution and dynamics, bacterial membrane and chromosomal structure in *Escherichia coli Methods Appl. Fluorescence* **3** 014005

[34] Endesfelder U *et al* 2013 Multiscale spatial organization of RNA polymerase in *Escherichia coli Biophys. J.* **105** 172–81

[35] Bakshi S *et al* 2013 Partitioning of RNA polymerase activity in live *Escherichia coli* from analysis of single-molecule diffusive trajectories *Biophys. J.* **105** 2676–86

[36] Bakshi S *et al* 2012 Superresolution imaging of ribosomes and RNA polymerase in live *Escherichia coli* cells *Mol. Microbiol.* **85** 21–38

[37] Virant D *et al* 2017 Combining primed photoconversion and UV-photoactivation for aberration-free, live-cell compliant multi-color single-molecule localization microscopy imaging *Int. J. Mol. Sci.* **18** 1–13

[38] Sperling R A *et al* 2008 Biological applications of gold nanoparticles *Chem. Soc. Rev.* **37** 1896–908

[39] Xiao L and Yeung E S 2014 Optical imaging of individual plasmonic nanoparticles in biological samples *Annu. Rev. Anal. Chem.* **7** 89–111

[40] Sengupta P, Jovanovic-Talisman T and Lippincott-Schwartz J 2013 Quantifying spatial organization in point-localization superresolution images using pair correlation analysis *Nat. Protocols* **8** 345–54

[41] Annibale P *et al* 2012 Identification of the factors affecting co-localization precision for quantitative multicolor localization microscopy *Opt. Nanoscopy* **1** 9

[42] Grimm J B *et al* 2015 A general method to improve fluorophores for live-cell and single-molecule microscopy *Nat. Methods* **12** 244–50